Detection and Quantification of Long-Range RNA Base Pairs in Coronavirus Genomes with SEARCH-MaP and SEISMIC-RNA

Introduction

Across all domains of life, RNA molecules perform myriad functions in development [1], immunity [2], epigenetics [3], cancer [4], sensing [5, 6], translation [7], and more. RNA also constitutes the genomes of many threatening viruses [8], including influenza viruses [9] and coronaviruses [10]. The capabilities of an RNA depend not only on its sequence (primary structure) but also on its base pairs (secondary structure) and three-dimensional shape (tertiary structure) [11].

High-quality tertiary structures provide more information than primary or secondary structures. However, nearly all RNA sequences fold into an ensemble of coexisting structures [12, 13]; resolving individual tertiary structures often proves difficult or impossible with mainstay methods used for proteins [14]. Consequently, the world's largest database of tertiary structures – the Protein Data Bank [15] – has accumulated only 1,839 structures of RNAs (compared to 198,506 of proteins) as of February 2024. Worse, most of those RNAs are short: only 119 are longer than 200 nt; and of those, only 24 are not ribosomal RNAs or group I/II introns. Due in part to the paucity of non-redundant long RNA structures, methods of predicting tertiary structures for RNAs lag far behind those for proteins [16].

The situation is only marginally better for RNA secondary structures. If a diverse set of homologous RNA sequences is available, a consensus secondary structure can often be predicted using comparative sequence analysis, which has proven accurate for ribosomal and transfer RNAs, among others [17]. An extension known as a covariance model [18] underlies the widely-used Rfam database [19] of consensus secondary structures for 4,170 RNA families (as of version 14.10). Although extensive, Rfam contains no protein-coding sequences (with rare exceptions such as frameshift stimulating elements) and provides one secondary structure for each family (while many RNAs fold into multiple functional structures [13]). Each family also represents only a short segment of a full RNA sequence; for coronaviruses, families exist for only the 5' and 3' untranslated regions, the frameshift stimulat-

ing element, and the packaging signal, which collectively constitute only 3% of the genomic RNA.

Predicting secondary structures faces two major obstacles due to the scarcity of high-quality RNA structures, particularly for RNAs longer than 200 nt including long non-coding [20], messenger [21], and viral genomic [22] RNAs. First, prediction methods trained on known RNA structures are limited to small, low-diversity training datasets (generally of short sequences), which causes overfitting and hence inaccurate predictions for dissimilar RNAs (including longer sequences) [23, 24]. Second, without known secondary structures of many diverse RNAs, the accuracy of any prediction method cannot be properly benchmarked [21, 25]. For these reasons, and because thermodynamic-based models also tend to be less accurate for longer RNAs [22] and base pairs spanning longer distances [26], predicting secondary structures of long RNAs remains unreliable.

The most promising methods for determining the structures of long RNAs employ experimental data. Chemical probing is a broad class of methods that involve treating RNA with reagents that modify nucleotides depending on the local secondary structure; for instance, dimethyl sulfate (DMS) methylates adenosine and cytidine residues only if they are not base-paired [27]. The latest approaches use reverse transcription to encode modifications to the RNA as mutations in the cDNA, followed by next-generation sequencing – a strategy known as mutational profiling (MaP) [28, 29]. A key advantage of MaP is that the sequencing reads can be clustered with DREEM [30] or DRACO [31] to detect multiple secondary structures in an ensemble. Determining the base pairs in those structures still requires structure prediction algorithms [32], although incorporating chemical probing data does improve accuracy [33, 34].

Several experimental methods have been developed to find base pairs directly, with minimal reliance on structure prediction. M2-seq [35] introduces random mutagenesis before chemical probing to detect correlated mutations between pairs of bases, which indicates the bases interact. Formation of alternative structures complicates the data analysis [36]. DANCE-MaP [37] was developed to find al-

ternative structures from M2-seq datasets via clustering; still, it can only find interactions between bases on the same read (typically up to 300 nt) and requires very high sequencing depth (over 1 million reads). For long-range base pairs, many methods involving crosslinking, proximity ligation, and sequencing have been developed [38]. These methods can find RNA–RNA interactions spanning arbitrarily long distances – as well as intermolecular RNA–RNA interactions – but nether achieve single-nucleotide resolution nor resolve alternative structures. Detecting, resolving, and quantifying alternative structures with base pairs that span arbitrarily long distances remains an open challenge.

Here, we introduce "Structure Ensemble Ablation by Reverse Complement Hybridization with Mutational Profiling" (SEARCH-MaP) to probe RNA–RNA interactions spanning arbitrarily large distances. We also develop the software "Structure Ensemble Inference by Sequencing, Mutation Identification, and Clustering of RNA" (SEISMIC-RNA) to analyze data from SEARCH-MaP (as well as DMS-MaPseq [29] and SHAPE-MaP [28]). Using SEARCH-MaP and SEISMIC-RNA, we discover and quantify an extensive set of long-range base pairs in the genome of SARS coronavirus 2. We show that this long-range structure inhibits the folding of a pseudoknot that stimulates ribosomal frameshifting [39, 40], hinting that it could regulate viral protein synthesis. We also discover homologous structures in other SARS-related viruses and other long-range base-pairing involving the frameshift elements of more dissimilar coronaviruses including transmissible gastroenteritis virus (TGEV). Finally, we model the full genomic secondary structure of live TGEV in ST cells and suggest other regions that form long-range base pairs. In addition to revealing new structures in coronaviral genomes, our findings show how SEARCH-MaP and SEISMIC-RNA can characterize secondary structure ensembles of long RNA molecules in general – a necessary step in developing a true "AlphaFold for RNA" [16].

Results

Strategy of SEARCH-MaP and SEISMIC-RNA

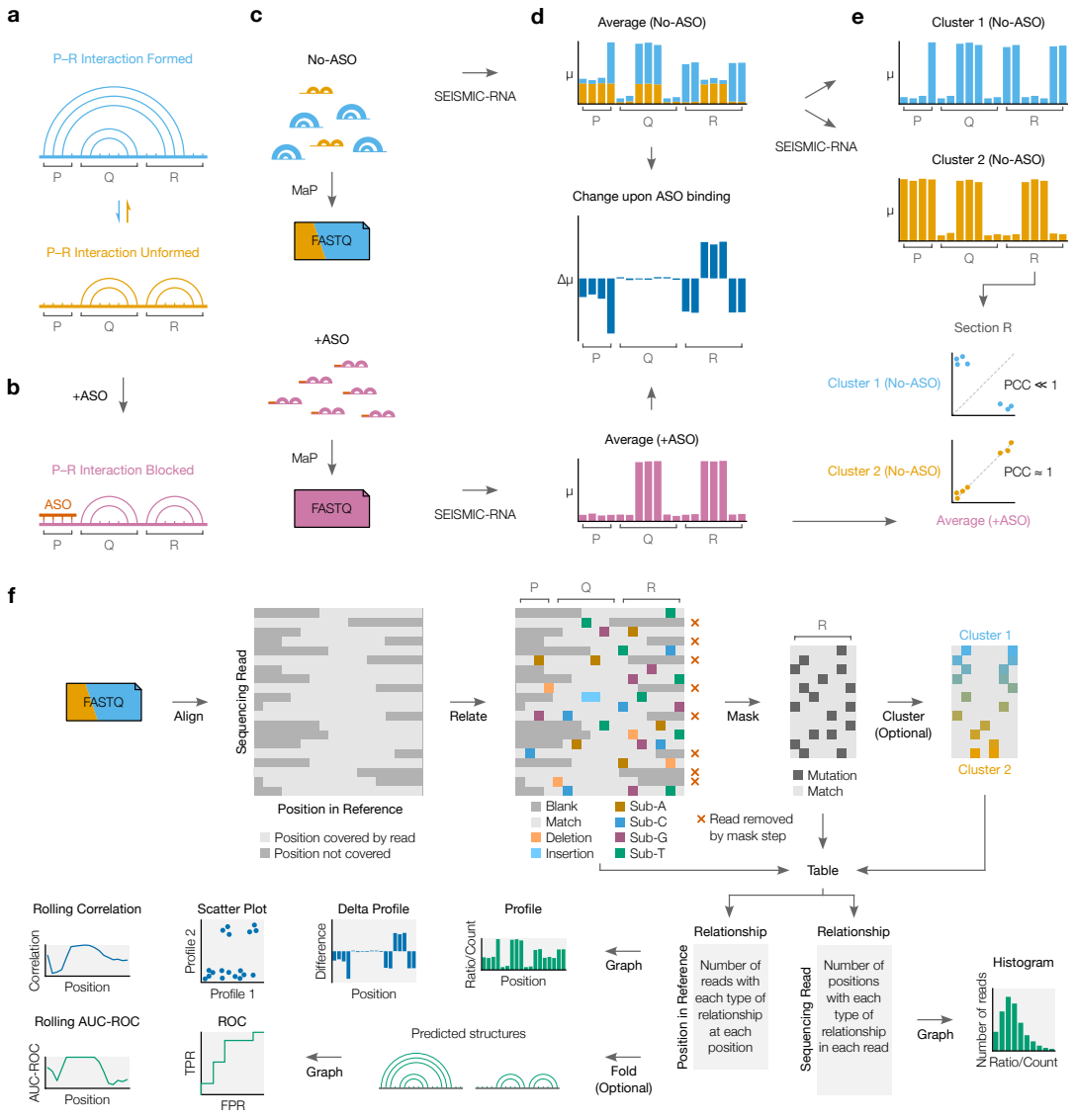

Figure 1: **The strategy of SEARCH-MaP and SEISMIC-RNA. (a)** This toy RNA is partitioned into three sections (P, Q, and R) whose molecules exist in two structural states: one in which an interaction between P and R forms and one in which it does not. **(b)** Hybridizing an ASO to P blocks it from interacting with R and forces all RNA molecules into the state where the P–R interaction is unformed. **(c)** A SEARCH-MaP experiment entails separate chemical probing and mutational profiling (MaP) with (+ASO) and without (No-ASO) the ASO, followed by sequencing to generate FASTQ files. The RNA molecules and FASTQ files use the same color scheme as in (a) and are illustrated/colored in proportion to their abundances in the ensemble. **(d)** Ensemble average mutational profiles with (+ASO) and without (No-ASO) the ASO, computed with SEISMIC-RNA. The *x*-axis is the position in the RNA sequence; the *y*-axis is the fraction of mutations (μ) at the position. Each bar in the No-ASO profile is drawn in two colors merely to illustrate how much each structural state contributes to each position; in a real experiment, states cannot be distinguished before clustering. The change upon ASO binding indicates the difference in the fraction of mutations ($\Delta\mu$) between the +ASO and No-ASO conditions.

We illustrate SEARCH-MaP with an RNA comprising three sections (P, Q, and R) that folds into an ensemble of two structural states: one in which a base-pairing interaction between P and R forms, another in which it does not (Figure 1a). Searching for sections that interact with P begins with hybridizing an antisense oligonucleotide (ASO) to P, which blocks P from base pairing with any other section, ablating the state in which the P–R interaction forms (Figure 1b). The RNA is chemically probed separately with (+ASO) and without (–ASO) the ASO, followed by mutational profiling and sequencing, e.g. using DMS-MaPseq [29] (Figure 1c).

SEISMIC-RNA can detect RNA–RNA interactions by comparing the +ASO and –ASO mutational profiles. Theoretically, each structural state has its own mutational profile [41], but the mutational profile of a single state is not directly observable because all states are physically mixed during the experiment (Figure 1c, top). Instead, the directly observable mutational profile is the "ensemble average" – the average of the states' (unobserved) mutational profiles, weighted by the states' (unobserved) proportions (Figure 1d, top). Because the structures – and therefore mutational profiles – of R differ between the interaction-formed and -unformed states, the ensemble averages of R also differ between the +ASO and –ASO conditions (Figure 1d, middle). However, this is not the case for element Q, which has the same secondary structure in both states (Figure 1d, middle). Therefore, one can deduce that P interacts with R – but not with Q – because hybridizing an ASO to P alters the mutational profile of R but not of Q.

After identifying RNA–RNA interactions, SEISMIC-RNA can also determine the mutational profiles of the states where the P–R interaction is formed and unformed – even if their secondary structures are unknown. Inferring mutational profiles for the interaction-formed and -unformed states requires clustering the –ASO ensemble into two clusters of RNA molecules (Figure 1e, top). Each cluster has its own mutational profile and corresponds to one structural state, but which cluster corresponds to the interaction-formed (or -unformed) state is not yet known. The interaction-unformed state has a mutational profile similar to that of the +ASO ensemble average, since the ASO blocks the interaction and forces the RNA into

the interaction-unformed state. Therefore, a cluster that correlates well ($r \approx 1$) with the +ASO ensemble average (here, Cluster 2) corresponds to the interaction-unformed state; while a cluster that correlates weakly ($r \ll 1$) corresponds to the interaction-formed state (Figure 1e, bottom).

SEARCH-MaP detects base-pairing in ribosomal RNA

We first validated SEARCH-MaP using 23S ribosomal RNA (rRNA) from *E. coli*. For each rRNA, we selected two RNA–RNA interactions that had been detected in a cell-free system [42]. Binding an ASO to either side of an interaction would block its formation, perturbing the structure of the other side (distant from the ASO binding site). Thus, for each interaction, we designed two ASOs, one targeting each side.

We folded the 23S rRNAs with each ASO, performed DMS-MaPseq over the entire transcripts, and compared ensemble average mutational profiles with and without ASOs using SEISMIC-RNA (Figure 2). Every ASO caused a prominent dip in the rolling Pearson correlation coefficient (PCC) at its target site and the immediate vicinity, confirming that each ASO bound properly to the RNA. The ASO targeting positions 1,647-1,668 also caused a smaller dip in PCC around positions 1,987-2,045 – coinciding with the 3' side of a stem whose 5' side was targeted by the ASO – showing that this interaction could be detected with SEARCH-MaP. Conversely, targeting the 3' side of this stem with an ASO binding positions 1,978-2,010 caused a small – though still above-baseline – dip in PCC around position 1,670 (near the stem's 5' side) and another around position 1,800 (the 5' side of another stem targeted by the ASO). Shifting the ASO slightly downstream to target positions 2,042-2,076 maintained the dips in PCC around 1,670 and 1,800 while introducing new dips around positions 2,245, 2,435, and 2,630, which correspond to the 3' sides of three stems within or close to the ASO target site. Binding an ASO to 2,429-2,452 – the 3' side of one such stem – caused the PCC to dip around position 2,055 at the 5' end of this stem. These results show that SEARCH-MaP could detect multiple stems ranging from 200 to 600 nt in 23S rRNA from *E. coli*.

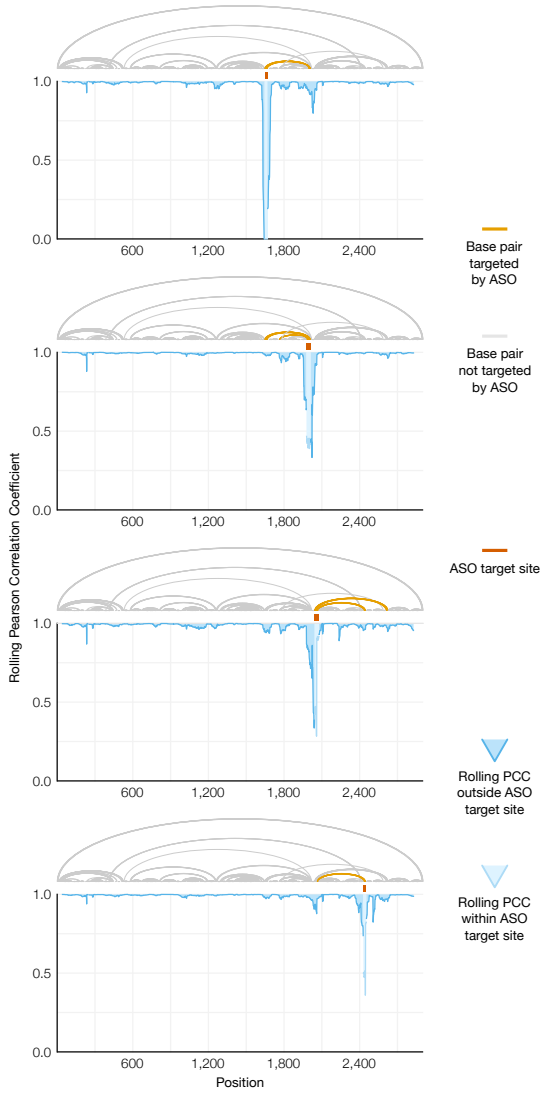

Figure 2: **Validation of SEARCH-MaP on 23S ribosomal RNA from *E. coli*.** Each graph shows the rolling (window = 45 nt) Pearson correlation coefficient (PCC) between the rRNA to which one ASO was added and a no-ASO control. The known secondary structure of the 23S rRNA [17] is drawn above the graph; base pairs with one side within the ASO target site are highlighted.

SEARCH-MaP detects, separates, and quantifies a long-range RNA–RNA interaction in SARS-CoV-2

Aside from ribosomes, many of the best-characterized functional long-range RNA–RNA interactions occur in the genomes of RNA viruses [43]. Coronaviruses regulate translation of their first open reading frame (ORF1) using programmed ribosomal frameshifting [44]. In the middle of ORF1, a switch called a frameshift stimulation element (FSE) makes a fraction of ribosomes slip backwards into the -1

reading frame. Ribosomes that maintain reading frame terminate at a stop codon shortly after the FSE, while those that frameshift bypass that stop codon and reach the end of ORF1. Why coronaviruses need a frameshifting mechanism remains an open question [45], yet all have FSEs [44].

Every coronaviral FSE contains a "slippery site" (UUUAAAC) and a structure characterized as a pseudoknot in multiple species [46, 47, 48]. Indeed, the isolated core of the SARS coronavirus 2 (SARS-CoV-2) FSE was shown to fold into a pseudoknot with three stems [40, 49, 50]. However, we discovered that when FSE is in its natural place in the SARS-CoV-2 genome, pseudoknot stem 1 is disassembled while an alternative stem 1 folds [51]. A 283 nt segment of the RNA genome – containing both the FSE and alternative stem 1 – failed to fully mimic the DMS reactivities of the full virus (PCC = 0.75). A 2,924 nt segment came closer (PCC = 0.93), suggesting that – only in the context of this longer sequence – the FSE adopts yet another structure, presumably a long-range interaction [51].

We used SEARCH-MaP to find the long-range interaction involving the FSE. We hypothesized it would turn out to be the structure another group had discovered and named the "FSE-arch" [52]. If so, the structure of the FSE would be perturbed by – and only by – ASOs targeting either side of the putative FSE-arch. To investigate, we added (separately) thirteen groups of DNA ASOs to the 2,924 nt segment (Figure 3a). Each group contained four or five ASOs targeting a contiguous 213-244 nt section of the RNA; target sites of adjacent groups abutted without overlapping. After adding each group of ASOs, we performed DMS-MaPseq with two pairs of RT-PCR primers: flanking the ASO target site (to confirm binding) and flanking the 5' FSE-arch (to detect structural changes). We obtained data for every ASO group except 13. All ASO groups bound properly, evidenced by suppression of DMS reactivities over their target sites (SFIG).

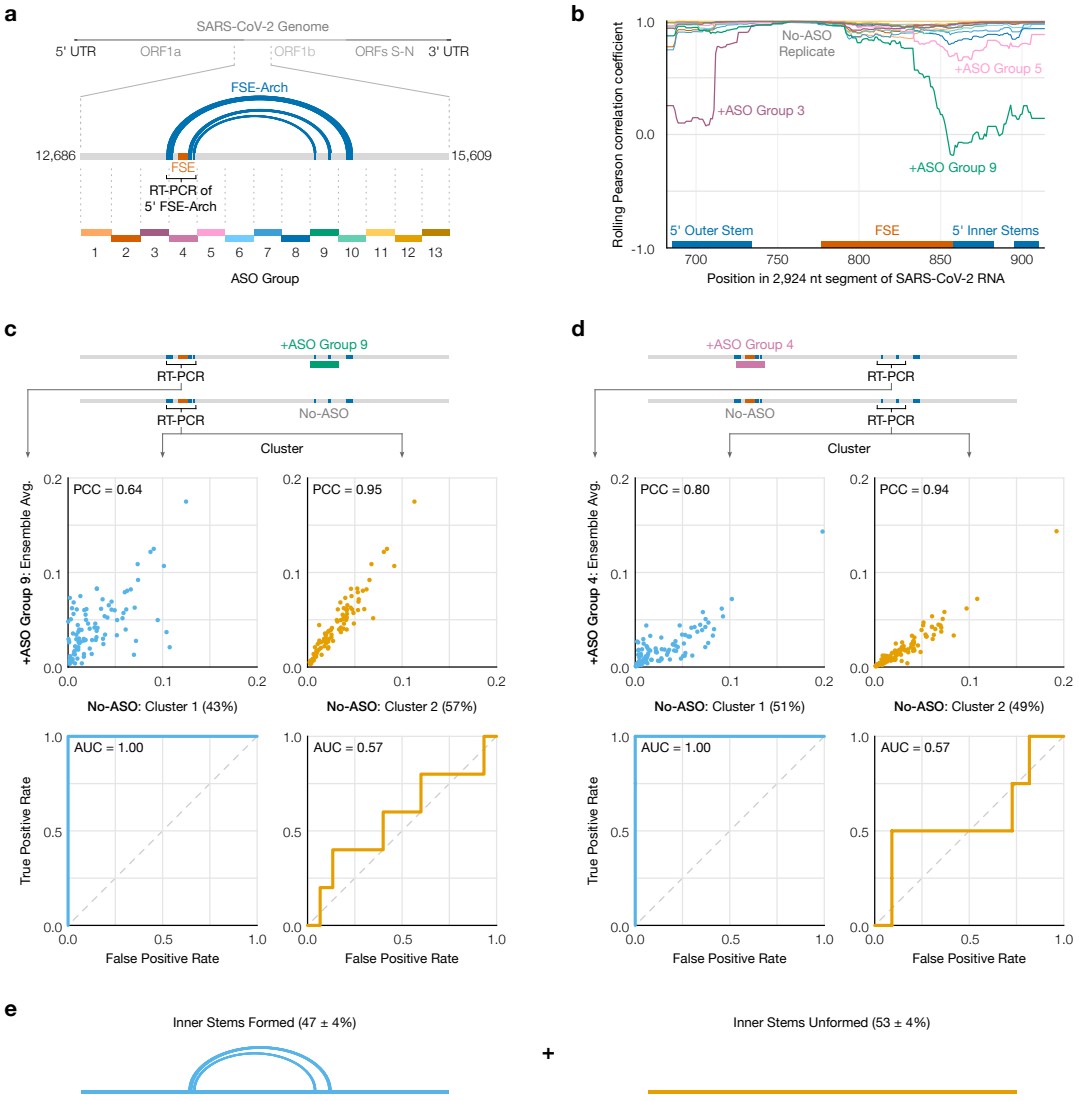

Figure 3: **Search for a long-range RNA–RNA interaction with the SARS-CoV-2 FSE. (a)** The 2,924 nt segment of the SARS-CoV-2 genome containing the frameshift stimulation element (FSE) and putative FSE-arch [52]. The target site of each ASO group is indicated by dotted lines; lengths are to scale. **(b)** Rolling (window = 45 nt) Pearson correlation coefficient of DMS reactivities over the 5' FSE-arch between each +ASO sample and a no-ASO control. Each curve represents one ASO group, colored as in (a); groups 4 and 13 are not shown. Locations of the FSE and the outer and inner stems of the 5' FSE-arch are also indicated. **(c)** (Top) Scatter plots of DMS reactivities over the 5' FSE-arch comparing each cluster of the no-ASO sample to the sample with ASO group 9; each point is one position in the 5' FSE-arch. (Bottom) Receiver operating characteristic (ROC) curves comparing each cluster of the no-ASO sample to the two inner stems of the FSE-arch. **(d)** Like (c) but over the 3' FSE-arch, and comparing to the sample with ASO group 4. One highly reactive outlier was ignored when calculating PCC. **(e)** Model of the inner two stems in the ensemble of structures formed by the 2,924 nt segment.

To quantify structural changes over the 5' FSE-arch, we calculated the rolling Pearson correlation coefficient (PCC) of the DMS reactivities between each sam-

ple and a no-ASO control (Figure 3b). A no-ASO replicate had a rolling PCC consistently between 0.93 and 1.00 (mean = 0.97), confirming the DMS reactivities were reproducible. ASO group 9 – targeting both 3' inner stems of the FSE-arch – caused the rolling PCC to dip below 0.5 over both 5' inner stems, exactly as expected if the inner stems of the FSE-arch existed. The only other ASO groups with substantial effects were 3, 4, and 5, which overlapped or abutted the FSE and presumably perturbed short-range base pairs; the outer stem of the FSE-arch (targeted by ASO group 10) did not apparently form. These results suggest both inner stems of the FSE-arch exist and are the predominant long-range interactions involving the immediate vicinity of the FSE.

We next sought to determine in what fraction of molecules the two inner stems of the FSE-arch form. Using SEISMIC-RNA, we clustered reads from the 5' side of the FSE-arch for the no-ASO control and found two clusters with a 43/57% split. To determine if they corresponded to the two inner stems formed and unformed, we compared their DMS reactivities to those after adding ASO group 9, which blocks the two inner stems (Figure 3c, top). Cluster 2 had similar DMS reactivities (PCC = 0.95), indicating it corresponds to the stems unformed. Meanwhile, the DMS reactivities of cluster 1 differed (PCC = 0.64), suggesting it corresponds to the stems formed.

To further support this result, we leveraged the preexisting model of the FSE-arch [52]. If cluster 1 did correspond to the two inner stems formed, we would expect its DMS reactivities to agree well with their structures (i.e. paired and unpaired bases should have low and high reactivities, respectively) and those of cluster 2 to agree much less. We quantified this agreement using receiver operating characteristic (ROC) curves (Figure 3c, bottom). The area under the curve (AUC) for cluster 1 was 1.00, indicating perfect agreement with the two inner stems of the FSE-arch; while that of cluster 2 was 0.57, close to null (0.50). This result further supports that cluster 1 (43%) corresponds to the two inner stems formed, and cluster 2 (57%) to these stems unformed.

If the RNA exists as an ensemble of the two inner stems formed and unformed, then we would also expect the 3' side of the FSE-arch to cluster into formed and unformed states. To investigate, we performed RT-PCR with primers flanking the 3' side of the inner two stems – both without ASOs and with ASO group 4 (targeting the 5' side of the FSE-arch). We clustered the no-ASO control into two clusters (51/49% split) and found – similar to the previous result – that the DMS reactivities after blocking the 5' FSE-arch with ASO group 4 resembled those of cluster 2 (PCC = 0.94) but not cluster 1 (PCC = 0.80), while the structure of the two inner stems agreed with cluster 1 (AUC = 1.00) but not cluster 2 (AUC = 0.57) (Figure 3d). We concluded that the RNA exists as an ensemble of structures in which the two inner stems of the FSE-arch form in 47% ± 4% of molecules (Figure 3e).

The long-range interaction competes with the frameshift pseudoknot in SARS-CoV-2

Having clustered out the DMS reactivities of the interaction-formed state on both sides of the FSE-arch (cluster 1 in Figure 3c and d), we used them as DMS constraints [33] in RNAstructure [32] to fold a 1,799 nt segment centered on the long-range interaction. This refined model (Figure 4) included not only the two inner stems of the FSE-arch – which we hereafter call long stems 1 (LS1) and 2 (LS2) – but also two stems (LS3 and LS4) that were not in the original FSE-arch model [52]. The structure also contained the alternative stem 1 (AS1) that we had previously discovered [51]. To our surprise, LS2b, LS3, and LS4 of the new model collectively overlapped all three stems of the pseudoknot (PS1, PS2, and PS3) that is generally thought to stimulate frameshifting [39, 40, 50]. Thus, these long stems – if they exist – and the pseudoknot would be mutually exclusive.

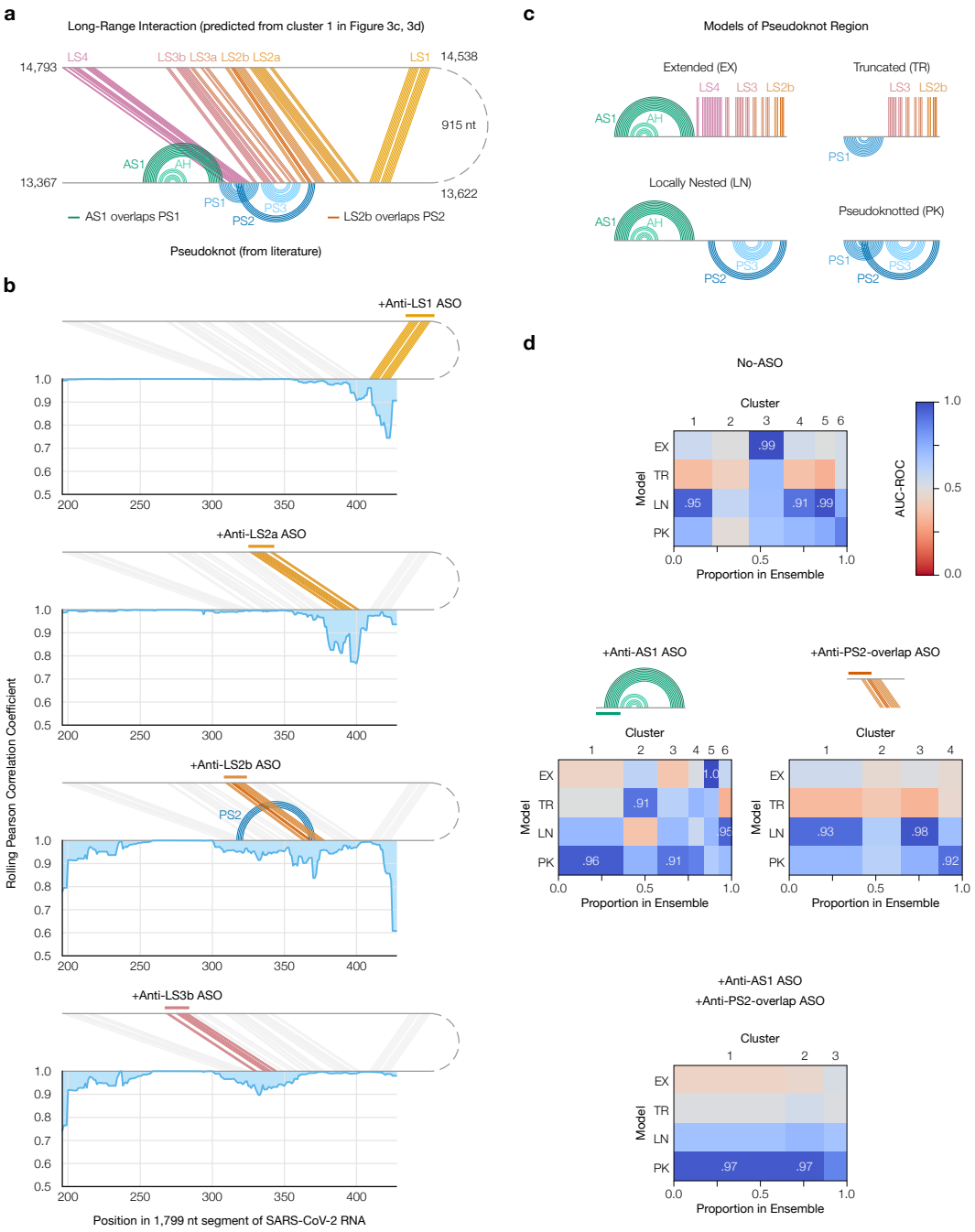

Figure 4: **Refinement of the long-range interaction and competition with the frameshift pseudoknot. (a)** Refined model of the long-range interaction (minimum free energy prediction based on cluster 1 in Figure 3c and d) including alternative stem 1 (AS1) [51]; the attenuator hairpin (AH) [53]; and long stems LS1, LS2a/b, LS3a/b, and LS4. Locations of pseudoknot stems PS1, PS2, and PS3 are also shown; as are the base pairs they overlap in AS1 and LS2b. **(b)** Rolling (window = 21 nt) Pearson correlation coefficient of DMS reactivities between each +ASO sample and a no-ASO control; base pairs targeted by each ASO are colored. **(c)** Models of possible structures for the FSE, by combining non-overlapping stems from (a). **(d)** Heatmaps comparing models in (c) to clusters of DMS reactivities over positions 305-371 via the area under the receiver operating characteristic curve (AUC-ROC). AUC-ROCs at least 0.90 are annotated. Cluster widths indicate proportions in the ensemble.

To verify this refined model, we performed SEARCH-MaP on the 1,799 nt segment using 15-20 nt LNA/DNA mixmer ASOs for single-stem precision (Figure 4b). Each ASO targeted one stem in the downstream portion of the interaction, and we measured the change in DMS reactivities of the FSE. ASOs targeting the 3' sides of LS1 and LS2a perturbed the DMS reactivities in exactly the expected locations on the 5' sides. Binding an ASO to the 3' side of LS2b caused a larger perturbation with more off-target effects, likely because this stem overlaps with pseudoknot stem 2 (PS2). Blocking LS3b also resulted in a main effect around the intended location, with one off-target effect upstream, suggesting that there may be another RNA–RNA interaction with the pseudoknot and this upstream region. Therefore, stems LS1, LS2a/b, and LS3b do exist – at least in a portion of the ensemble.

We then sought to determine whether the long-range stems compete with the pseudoknot. If so, blocking them with ASOs would increase the proportion of the pseudoknot in the ensemble. To test this hypothesis, we first generated four possible models of the FSE structure by combining mutually compatible stems from the refined model (Figure 4c). Then, we clustered the 1,799 nt segment without ASOs up to 6 clusters (the maximum number reproducible between replicates) and compared each cluster to each structure model using the area under the receiver operating characteristic curve (AUC-ROC) over the positions spanned by the pseudoknot, 305-371 (Figure 4d, top). We considered a cluster and model to be consistent if the AUC-ROC was at least 0.90. The locally nested model (AS1 plus PS2 and PS3) was consistent with three clusters totaling 52% of the ensemble, while the extended model (AS1 plus all long-range stems) was consistent with one cluster (20%). No clusters were fully consistent with the pseudoknotted model, though the least-abundant cluster (7%) came close with an AUC-ROC of 0.88. The remaining cluster (21%) was not consistent with any model, suggesting that the ensemble contains structures beyond those in Figure 4c.

Adding an ASO targeting the 5' side of AS1 reduced the proportion of AS1-containing states (extended and locally nested) from 72% to 16% (Figure 4d, left). In their absence emerged clusters consistent with the pseudoknotted and trun-

cated models, representing 56% and 20% of the ensemble, respectively. Meanwhile, adding an ASO that blocked the part of LS2b that overlaps PS2 eliminated the extended state (which includes LS2b) and produced one cluster (13%) consistent with the pseudoknotted model (Figure 4d, right). Adding both ASOs simultaneously collapsed the ensemble into three clusters of which two (87%) were highly consistent with the pseudoknotted model (Figure 4d, bottom). Since blocking the PS2-overlapping portion of LS2b increased the proportion of clusters consistent (or nearly so) with the pseudoknotted model – both alone and combined with the anti-AS1 ASO – we conclude that the long-range interaction does outcompete the pseudoknot.

Frameshift stimulating elements of multiple coronaviruses participate in long-range RNA–RNA interactions

We surmised that other coronaviruses would also feature long-range RNA–RNA interactions involving the FSE. To search for such structures, we performed SEARCH-MaP with FSE-targeted ASOs on 1,799 nt segments from eight coronaviral genomes.

Computational and experimental screening identifies eight coronaviruses with potential long-range interactions

As of December 2021, the NCBI Reference Sequence Database [54] contained 62 complete genomes of coronaviruses. To focus on those likely to have long-range interactions involving the FSE, we predicted the likelihood that each base in a 2,000 nt section surrounding the FSE would pair with a base in the FSE (SFIG). Based on these predicted interactions, we selected ten coronaviruses – at least one from each genus (SFIG) – including SARS-CoV-2 as a positive control. Within the genus *Betacoronavirus*, we included all three SARS-related viruses – SARS coro-

naviruses 1 (NC_004718.3) and 2 (NC_045512.2) and bat coronavirus BM48-31 (NC_014470.1) – because they clustered into their own structural outgroup. The other three strains of *Betacoronavirus* that we selected were MERS coronavirus (NC_019843.3) with a predicted interaction at positions 510-530; and human coronavirus OC43 (NC_006213.1) and murine hepatitis virus strain A59 (NC_048217.1), both with a predicted upstream interaction at positions 10-20. We selected two strains of *Alphacoronavirus*: transmissible gastroenteritis virus (NC_038861.1) and bat coronavirus 1A (NC_010437.1), predicted to have interactions at positions 440-460 and 350-360, respectively. Avian infectious bronchitis virus strain Beaudette (NC_001451.1) – a strain of *Gammacoronavirus* – was predicted to have a strong interaction at positions 330-350, while common moorhen coronavirus HKU21 (NC_016996.1) was the species of *Deltacoronavirus* with the most promising FSE interactions.

We reasoned that if an FSE does interact with a distant RNA element, removing that element by truncating the RNA would change the structure of the FSE, which we could detect with DMS-MaPseq. For each of the ten coronaviruses that passed the computational screen, we *in vitro* transcribed and performed DMS-MaPseq [29] on both a 239 nt segment comprising the FSE and minimal flanking sequences and a 1,799 nt segment encompassing the FSE and all sites with which it was predicted to interact. All coronaviruses except for human coronavirus OC43 and MERS coronavirus showed differences in their DMS reactivity profiles between the 239 nt and 1,799 nt segments (SFIG), suggesting long-range interactions involving the FSE.

SEARCH-MaP reveals long-range interactions involving the FSE in four additional coronaviruses

To determine which RNA elements the FSE base-pairs with in each coronavirus, we performed SEARCH-MaP on the 1,799 nt RNA segment using DNA ASOs targeting the vicinity of the FSE (Figure 5). The rolling Spearman correlation coefficient (SCC) between the +ASO and no-ASO mutational profiles dipped below 0.9 at the ASO

target site in every coronavirus segment, confirming the ASOs bound and altered the structure.

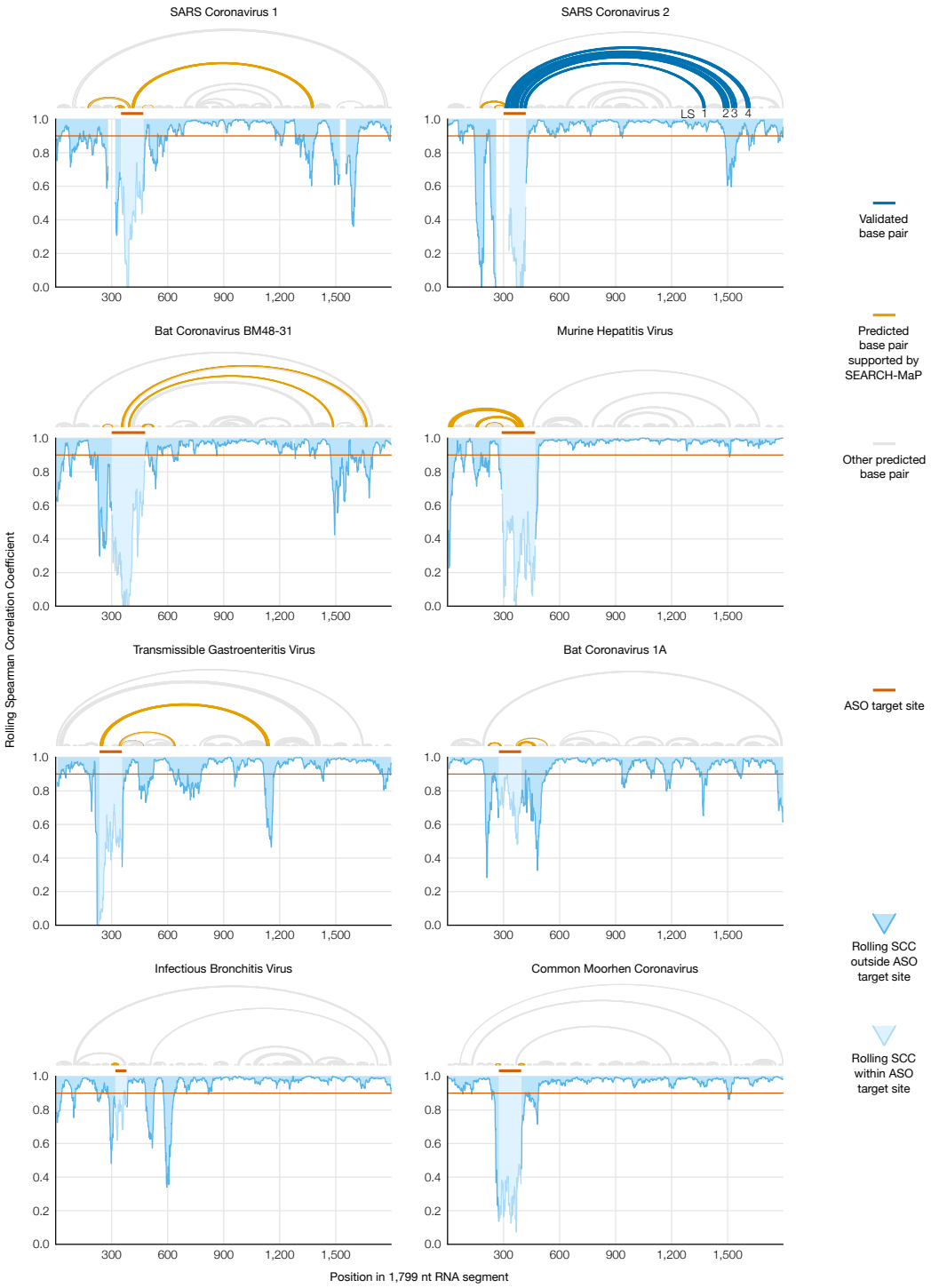

Figure 5: **Evidence for long-range RNA–RNA interactions involving the FSE in five coronaviruses.** Rolling (window = 45 nt) Spearman correlation coefficient (SCC) of DMS reactivities between the +ASO and no-ASO samples for each 1,799 nt segment of a coronaviral genome. The target site of each ASO is highlighted on the SCC data and shown above each graph. Structures predicted with RNAstructure [**?**] using no-ASO ensemble average DMS reactivities as constraints [33] are drawn above each graph; base pairs connecting the ASO target site to an off-target position with SCC less than 0.9 are colored. For SARS-CoV-2, the refined model (Figure 4a) is also drawn, with LS1-LS4 labeled.

To confirm we could detect long-range interactions, we compared the rolling SCC for the SARS-CoV-2 segment to our refined model of the long-range interaction (Figure 5, blue). The SCC dipped below 0.9 at positions 1,483-1,560 and at 1,611-1,642, which coincide with stems LS2-LS3 (positions 1,476-1,550 within the 1,799 nt segment) and stem LS4 (positions 1,600-1,622). These dips were the two largest downstream of the FSE; although others (corresponding to no known base pairs) existed, they were barely below 0.9 and could have resulted from base pairing between these regions and other (non-FSE) regions. Near LS1 (positions 1,367-1,381), the SCC dipped only slightly to a minimum of 0.95, presumably because LS1 is the smallest (15 nt) and most isolated long-range stem. Therefore, this method was sensitive enough to detect all but the smallest long-range stem, and specific enough that the two largest dips corresponded to validated base pairs.

We found similar long-range interactions in SARS-CoV-1 and another SARS-related virus, bat coronavirus BM48-31. Both viruses showed dips in SCC at roughly the same positions as LS2-LS4 in SARS-CoV-2, indicating that they have homologous structures. SARS-CoV-1 also had a wide dip below 0.9 at positions 1,284-1,394, corresponding to a homologous LS1. Thus, three SARS-related viruses share this multi-stemmed long-range interaction involving the FSE, hinting that this structure is functional.

In every other species except common moorhen coronavirus, we found prominent dips in SCC at least 200 nt from the ASO target site. To model potential base pairing between these dip positions and the FSE, we used the Fold program from RNAstructure [32] with the no-ASO ensemble average DMS reactivities as constraints [33]. We surmised that using DMS reactivities of clusters corresponding to long-range interactions would generally yield more accurate predictions of long-range interactions than would ensemble averages (over all structural states). For instance, the prediction for SARS-CoV-2 based on the ensemble average included LS1 and LS2b but missed the other long-range stems. Although clustered data were unavailable in this case, we were still able to find long-range base pairs consistent with the SEARCH-MaP data for both murine hepatitis virus and trans-

missible gastroenteritis virus (Figure 5, orange). We conclude that long-range interactions involving the FSE occur more widely than in just SARS-CoV-2, including in the genus *Alphacoronavirus*.

Structure of the full TGEV genome based on DMS-MaPseq supports a long-range RNA–RNA interaction involving the FSE

Transmissible gastroenteritis virus (TGEV) is a strain of *Alphacoronavirus 1* [55] that infects pigs and causes vomiting and diarrhea – almost always fatally in baby piglets [56]. Due to the impacts of TGEV on animal health and economics [56] and our evidence of a long-range RNA–RNA interaction, we sought to model the genomic secondary structures of live TGEV. We began by treating TGEV-infected ST cells with DMS (two biological replicates) and performing DMS-MaPseq (two technical replicates per biological replicate) on the extracted RNA (Figure 6a). The DMS reactivities over the full genome were consistent between biological replicates (PCC = 0.97), albeit not with the 1,799 nt segment *in vitro* (PCC = 0.82), which showed that verifying the long-range interaction in live virus would be necessary (Supplementary Figure 1).

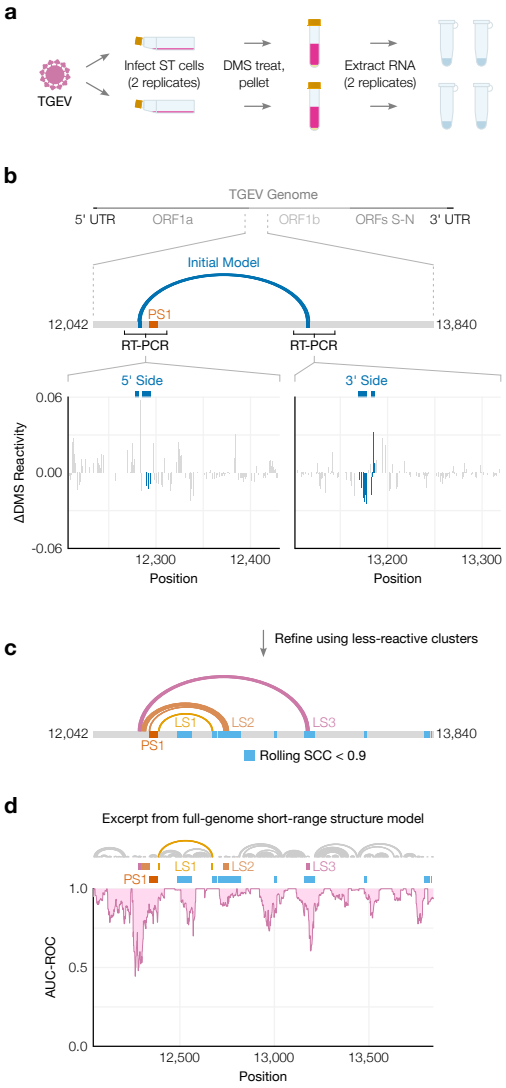

Figure 6: **Genomic secondary structure of live TGEV. (a)** Schematic of the experiment in which two biological replicates of ST cells were infected with TGEV, DMS-treated, and pelleted. Cell pellets were divided into two technical replicates prior to extraction of DMS-modified RNA. **(b)** Differences in DMS reactivities between the two clusters on each side of the long-range interaction. Each bar represents one base. Bases are shaded dark blue if they interact in the initial model of the long-range interaction (from Figure 5), shown above along with its location in the full genome. The locations of FSE pseudoknot stem 1 (PS1) and the regions amplified for clustering are also indicated. **(c)** Refined model of the long-range interaction in TGEV based on the DMS reactivities of the less-reactive cluster from both sides. Long stems 1 (LS1), 2 (LS2), and 3 (LS3) are labeled. For comparison with the regions of the 1,799 nt segment perturbed by the ASO (Figure 5), positions after the FSE where the SCC dipped below 0.9 are shaded light blue. **(d)** Rolling AUC-ROC (window = 45 nt) between the full-genome DMS reactivities and full-genome secondary structure modeled from the DMS reactivities (maximum 300 nt between paired bases). The structure model is drawn above the graph. Only positions 12,042-13,840 are shown here. For comparison, the locations of PS1, LS1, LS2, LS3, and dips in SCC after the FSE are also indicated.

To determine the structure ensembles, we performed RT-PCR on the extracted RNA using primers targeting both sides of the long-range interaction. The ensemble average DMS reactivities were consistent with those over the full genome (Supplementary Figure). For each side of the long-range interaction, we clustered the reads into two clusters (Figure 6b). These clusters had similar correlations with the +ASO sample and similar AUC-ROC scores (Supplementary Figure), making it more difficult to identify them for TGEV than for SARS-CoV-2 (Figure **??**). Nevertheless, we realized that on each side, the bases that were predicted to interact had generally lower DMS reactivities in one cluster compared to the other cluster, and hypothesized that this cluster corresponded to the long-range interaction (Figure 6b). On the 5' side, the less-reactive cluster constituted 52% of the ensemble; on the 3' side, 60%. To investigate, we refined the structure of the 1,799 nt segment using the DMS reactivities from both of these clusters. Consistent with our hypothesis, the minimum free energy (MFE) model included the long-range interaction, which we hereafter call long stem 3 (LS3) (Figure 6c); predicting the structure using both more-reactive clusters did not produce LS3 (Supplementary Figure). The refined model also featured a prominent new interaction connecting 20 nt upstream of the FSE with 400 nt downstream, which we call LS2. We suspect that LS2 exists because it coincides with a broad region perturbed by adding an ASO to the FSE in the 1,799 nt segment of TGEV (Figure 6c). Another stem spanning just under 300 nt, which we call LS1, was also predicted in the same location as in the 1,799 nt segment.

We used the ensemble average DMS reactivities to produce one "ensemble average" model of the secondary structure of the full TGEV genome (SUPPLEMENTARY FIGURE). We restricted base pairs to a maximum distance of 300 nt to make the computation tractable and avoid over-predicting spurious long-range interactions. To verify the model quality, we confirmed that the predicted structure of the first 520 nt included the highly conserved stem loops SL1, SL2, SL4, and SL5a/b/c in the 5' UTR [10] (Supplementary Figure 2a) and was consistent with the DMS reactivities (AUC-ROC = 0.94) (Supplementary Figure 2b).

The AUC-ROC was lower in many locations throughout the rest of the genome (Supplementary Figure), indicating that a single secondary structure consistent with the ensemble average DMS reactivities could not be found. We had noticed a similar phenomenon in SARS-CoV-2 – in particular, at the FSE [51]. Thus, we surmised that regions with low AUC-ROC scores likely form alternative structures or long-range interactions – or both – that a single secondary structure model could not capture. Checking if this relationship also held for TGEV, we found a large dip in AUC-ROC just upstream of the FSE, centered on the 5' ends of LS2 and LS3, as well as smaller dips at the 3' ends of both stems (Figure 6d). In fact, at or near every location that SEARCH-MaP had evidenced to interact with the FSE – where the rolling SCC had dipped – the AUC-ROC also dipped. This finding supports the hypothesis that long-range interactions and/or alternative structures are often the reason why predicted structures are not locally consistent with the DMS reactivities on which they were based.

Discussion

In this work, we developed SEARCH-MaP and SEISMIC-RNA and applied them jointly to detect structural ensembles involving long-range RNA:RNA interactions in SARS-CoV-2 and other coronaviruses. This study is certainly not the first to perturb RNA structure with ASOs, nor even the first to use DMS-MaPseq to quantify the structural changes upon binding ASOs to SARS-CoV-2 RNA [57]. But while this previous study examined local structural perturbations caused by binding an ASO, we show that we can detect changes in the structure at more distant locations in an RNA molecule that interact with the nucleotides bound by an ASO.

A previous study detected two long-range RNA–RNA interactions in the genome of satellite tobacco mosaic virus by binding an ASO (in this case, an LNA 9-mer) to each site, followed by chemical probing [58]. However, SEARCH-MaP and SEISMIC-RNA go further by also determining the mutational profile and proportion of the interaction-formed and -unformed states (Figure 3c, d). With a collection of candidate structure models, these methods even reveal how adding an ASO ablates specific structures, collapsing the ensemble into one predominant structure (Figure 4d).

Many methods have been developed to find long-range (and intermolecular) RNA–RNA base pairing using crosslinking (with psoralen or a derivative), proximity ligation, and deep sequencing [59, 60, 61, 62]. These methods require no prior knowledge of RNA–RNA interactions and have no limit to the length of the interactions they can detect. They do, however, suffer from several limitations including inefficient ligation [QUANTIFY, I think I read that less than 5% of molecules actually ligate] necessitating either enrichment or very deep sequencing, as well as bias towards U-rich sequences. They are not single-molecule techniques, either, meaning that although they can detect mutually exclusive base pairs, they cannot determine which specific alternative structures exist or quantify their proportions, as SEARCH-MaP/SEISMIC-RNA can. There is also no straightforward way to focus on one specific RNA–RNA interaction.

Another method based on applying many ASO ”patches” in parallel and reading out the signal with microarray probes has also recently been developed [63]. Like proximity ligation, this method has no limitation to the length of the interactions it could find, yet it is also not a single-molecule technique, meaning that it cannot resolve individual structures in an ensemble.

Could be possible to use SEARCH-MaP to evaluate the accuracy of computational predictions of RNA structures, especially for long-range base pairing. Also to generate a set of well-characterized secondary structures for developing new tools to predict RNA structures.

SEARCH-MaP bears conceptual similarity to another method, mutate-and-map read out through next-generation sequencing (M2-seq) [35]. Both involve perturbing one region of an RNA molecule (in the case of M2-seq, by pre-installing mutations through error-prone PCR) and measuring the effects on other bases in the RNA using chemical probing. The major differences are the precision and scale of the interactions identified, as well as the throughput. M2-seq can pinpoint interactions down to the resolution of a single base pair, and is thus more precise than SEARCH-MaP. However, DMS-guided RNA structure prediction can propose structure models at single-base-pair resolution, which SEARCH-MaP can validate, and in this way achieve single-base-pair resolution. SEARCH-MaP is also capable of finding interactions over a much longer range because M2-seq requires the interacting bases to be in the same Illumina sequencing read. Within this length limit, one M2-seq experiment can theoretically find all pairwise interactions between bases, while one SEARCH-MaP experiment can find only interactions that involve the region to which the ASOs were hybridized. M2-seq is also limited by the formation of alternative structures. Some methods, such as [CITE something by Rhiju, maybe REEFIT] and DANCE-MaP [37], have been designed to work around this limitation SEARCH-MaP; however, [something by Rhiju] has [this problem], and DANCE-MaP requires extremely high sequencing depth of several million reads [MORE PRECISE]. SEARCH-MaP, by contrast, assumes from the start that the RNA may form alternative structures; for simply detecting long-range interactions, even

a 5,000 read depth is sufficient coverage; and for clustering, we have found [SOME LIMIT].

Another limitation of SEARCH-MaP as presented here is that it cannot distinguish between direct and indirect interactions. If RNA segment A interacts with segment B, while B interacts with both segment A and C, then hybridizing an ASO to segment A would perturb the structure of B, which could consequentially perturb the structure of C. Hence, C would appear to interact with A, even though this interaction is indirect, through B. One possible workaround (not shown in this study) would be to mutate or hybridize an ASO to segment B, and then repeat the experiment with hybridizing an ASO to segment A. If the interaction between A and C is direct, then C should still be perturbed even when segment B is incapable of interacting with A or C. But if B mediates an indirect interaction between A and C, then disrupting B should eliminate the apparent interaction between A and C.

Functional long-range interactions up to four kilobases involving an FSE have been been found previously in two plant viruses [64, 65]. In both cases, frameshifting required the long-range interaction, suggesting that this interaction enables negative feedback on synthesis of viral RNA polymerase [64]. When polymerase levels are low, the interaction would form and stimulate frameshifting, which is needed to synthesize RNA polymerase. Once the polymerase had accumulated, it would begin to replicate the genomic RNA; in its passage from the genomic 3' end to the 5' end, it would disrupt the 3' side of the long-range interaction, attenuating frameshifting and reducing synthesis of more polymerase.

However, this strategy cannot be the role, if any, of the long-range interactions in coronaviruses. Unlike in the two plant viruses, a long-range interaction is not required to stimulate frameshifting in coronaviruses: numerous studies have shown that even the isolated FSE can cause 15 - 40% of ribosomes to frameshift [66, 67, 39, 51, 68, 69, 40]. In coronaviruses, the long-range interaction is not only unnecessary for frameshifting but also may even attenuate it, given that in SARS-CoV-2, the FSE-arch and the frameshift-stimulating pseudoknot seem to be mutually exclusive. Moreover, coronaviruses partition translation and RNA

synthesis into two different cellular compartments (the cytosol and the double-membrane vesicles, respectively) [70], so structural changes induced by RNA polymerases would not be seen by ribosomes. If any of the long stems existed, they would block the pseudoknot from forming, which suggests a mechanism by which the long-range interaction could regulate the structure – and possibly frameshifting activity – of the FSE. Although we had previously shown that AS1 overlaps and outcompetes PS1 [51], AS1 lies upstream of the slippery site and would be unwound by approaching ribosomes, while the long stems lie downstream and would not.

The functions of these long-range interactions involving the FSE in coronaviruses remain mysterious. However, given that they occur in multiple coronaviruses across at least two genera, it seems reasonable that they could play a role in the viral life cycle, possibly by affecting the rate of frameshifting. Further research may reveal new mechanisms of translational regulation in coronaviruses via long-range RNA:RNA interactions.

The emergence of coronavirus disease 2019 (COVID-19) as a pandemic in 2020 spurred many investigations on functional RNA structures in coronaviruses, particularly SARS coronavirus 2 (SARS-CoV-2) [71, 72, 52, 73, 74, 75, 76, 31, 77, 51]. Among the more unexpected findings was an RNA:RNA interaction between the frameshifting stimulation element (FSE) and another sequence up to 1,475 nt downstream, which the authors named the FSE-arch [52]. The FSE-arch was detected in infected cells using COMRADES [62] and proposed to comprise three nested long-range RNA:RNA interactions (Figure **??**a): an outer 38 bp bulged stem spanning coordinates 13,370-14,842 (which encompasses the FSE); a middle 18 bp bulged stem spanning coordinates 13,533-14,673; and an inner 14 bp bulged stem spanning coordinates 13,580-14,552 [52]. We had discovered that the FSE folds into at least two alternative structures in infected cells, in roughly equal proportions, and that the predicted structure for one of them resembles the FSE-arch [51]. Because computational RNA structure prediction – even guided by chemical prob-

ing data – is unreliable for long RNA sequences especially [78], we sought stronger, hypothesis-driven evidence for the existence of the FSE-arch.

Methods

Screening coronavirus long-range interactions computationally

All coronaviruses with reference genomes in the NCBI Reference Sequence Database [54] were searched for using the following query:

```
refseq[filter] AND ("Alphacoronavirus"[Organism] OR
                    "Betacoronavirus"[Organism] OR
                    "Gammacoronavirus"[Organism] OR
                    "Deltacoronavirus"[Organism])
```

The complete record of every reference genome was downloaded both in FASTA format (for the reference sequence) and in Feature Table format (for feature locations). The location of the frameshift stimulating element (FSE) in each genome was estimated from the feature table, and the nearest instance of `TTTAAAC` was used as the slippery site, using a custom Python script. The 2,000 nt segment beginning 100 nt upstream of and ending 1,893 nt downstream of the slippery site was used for predicting long-range interactions involving the FSE. Genomes with ambiguous nucleotides (e.g. `N`) in this segment were discarded. For each coronavirus genome, up to 100 secondary structure models of the 2,000 nt segment were generated using Fold version 6.3 from RNAstructure [32] with `-M 100` and otherwise default parameters. Then, for each position, the fraction of models for the coronavirus in which the base at the position paired with any other base between positions 101 (the first base of the slippery sequence) and 250 was calculated using a custom Python script. The coronaviruses were clustered by their fraction vectors using the unweighted pair group method with arithmetic mean (UPGMA) and a euclidean distance metric, implemented in Seaborn version 0.11 [79] and SciPy version 1.7 [80]. The resulting hierarchically-clustered heatmap was examined manually to select

coronaviruses based on the prominence of potential long-range interactions with the FSE (relatively large fractions far from positions 101-250).

Supplementary Figures

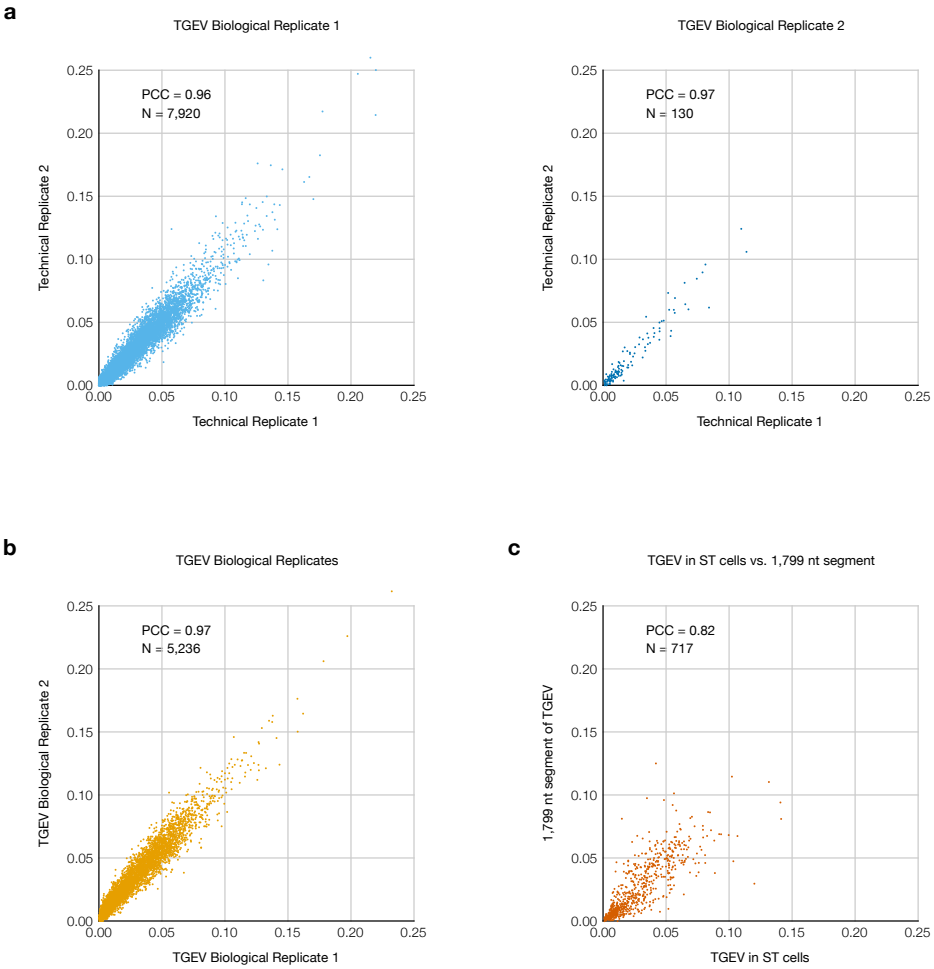

Supplementary Figure 1: **Replicates of TGEV in ST cells and comparison to the 1,799 nt segment. (a)** Scatter plots comparing the DMS reactivities of the two technical replicates for each biological replicate of TGEV in ST cells. Each point represents one base in the sequence. The number of points (N) and Pearson correlation coefficient (PCC) are indicated for each plot. **(b)** Scatter plot comparing the DMS reactivities of the two biological replicates (each biological replicate comprises the reads for both of its technical replicates pooled together). **(c)** Scatter plot comparing the DMS reactivities of TGEV in ST cells (the reads for both biological replicates pooled together) and for the 1,799 nt segment *in vitro*.

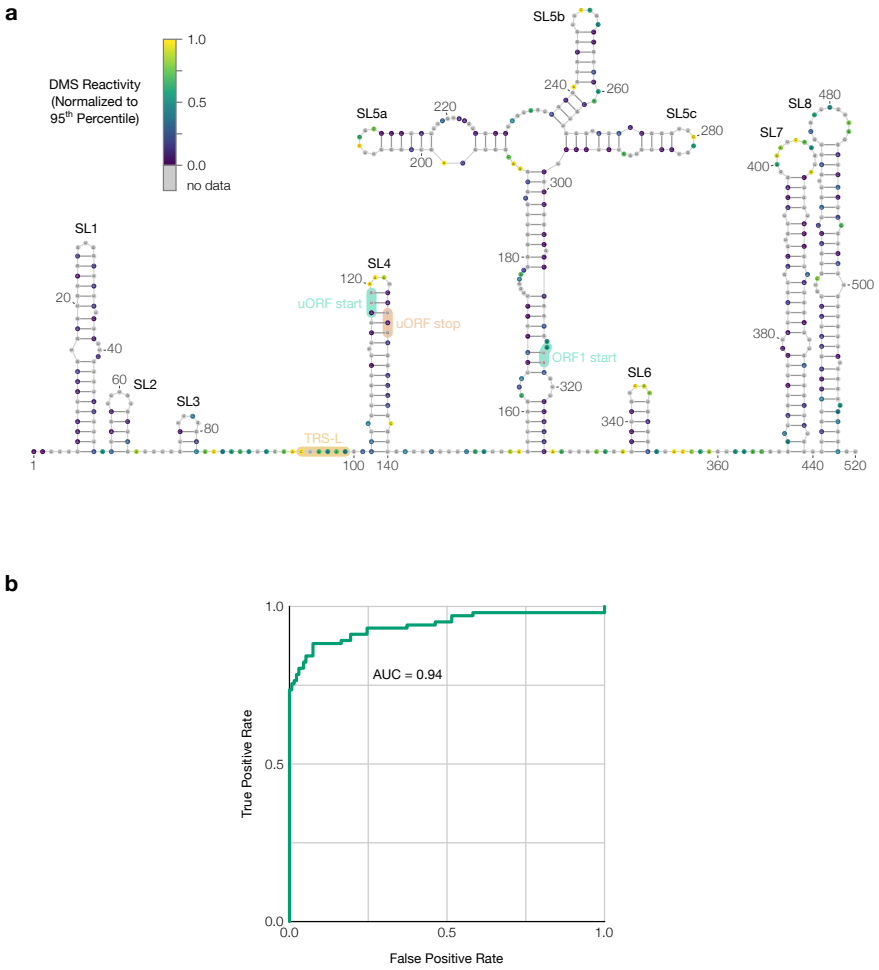

Supplementary Figure 2: **Secondary structure of the 5' UTR of transmissible gastroenteritis virus. (a)** Model of the secondary structure of the first 520 nt of the TGEV genome, based on DMS reactivities in infected ST cells normalized to the 95th percentile. Bases are colored by DMS reactivity. The model includes the highly conserved stem loops SL1, SL2, SL4, SL5a, SL5b, and SL5c, as well as the more variable stem loops SL3, SL6, SL7, and SL8 [10]. The leader transcription regulatory sequence (TRS-L) [81], upstream open reading frame (uORF) [82], and start codon of ORF1 are also labeled. The model was drawn using VARNA [83]. **(b)** Receiver operating characteristic curve showing agreement between the DMS reactivities and the secondary structure model; the area under the curve (AUC) is indicated.

References

[1] Carla A. Klattenhoff, Johanna C. Scheuermann, Lauren E. Surface, Robert K. Bradley, Paul A. Fields, Matthew L. Steinhauser, Huiming Ding, Vincent L. Butty, Lillian Torrey, Simon Haas, Ryan Abo, Mohammadsharif Tabebordbar, Richard T. Lee, Christopher B. Burge, and Laurie A. Boyer. Braveheart, a long noncoding rna required for cardiovascular lineage commitment. *Cell*, 152:570–583, 2013.

[2] Blake Wiedenheft, Samuel H. Sternberg, and Jennifer A. Doudna. Rna-guided genetic silencing systems in bacteria and archaea. *Nature*, 482(7385):331–338, 2012.

[3] Arunoday Bhan and Subhrangsu S. Mandal. Lncrna hotair: A master regulator of chromatin dynamics and cancer. *Biochimica et Biophysica Acta (BBA) - Reviews on Cancer*, 1856(1):151–164, 2015.

[4] Mohammadreza Hajjari and Adrian Salavaty. Hotair: an oncogenic long noncoding rna in different cancers. *Cancer Biol Med*, 12(1):1–9, Mar 2015.

[5] Jens Kortmann and Franz Narberhaus. Bacterial rna thermometers: molecular zippers and switches. *Nature Reviews Microbiology*, 10(4):255–265, 2012.

[6] Alexander Serganov and Evgeny Nudler. A decade of riboswitches. *Cell*, 152:17–24, 2013.

[7] Harry F Noller. Evolution of protein synthesis from an rna world. *Cold Spring Harb Perspect Biol*, 4(4):a003681, Apr 2012.

[8] Mark E. J. Woolhouse and Liam Brierley. Epidemiological characteristics of human-infective rna viruses. *Scientific Data*, 5(1):180017, 2018.

[9] Nicole M. Bouvier and Peter Palese. The biology of influenza viruses. *Vaccine*, 26:D49–D53, 2008. Influenza Vaccines: Research, Development and Public Health Challenges.

[10] Dong Yang and Julian L. Leibowitz. The structure and functions of coronavirus genomic 3' and 5' ends. *Virus Research*, 206:120–133, 2015.

[11] Stefanie A. Mortimer, Mary Anne Kidwell, and Jennifer A. Doudna. Insights into rna structure and function from genome-wide studies. *Nature Reviews Genetics*, 15(7):469–479, 2014.

[12] Anthony M. Mustoe, Charles L. Brooks, and Hashim M. Al-Hashimi. Hierarchy of rna functional dynamics. *Annual Review of Biochemistry*, 83(1):441–466, 2014. PMID: 24606137.

[13] Robert C. Spitale and Danny Incarnato. Probing the dynamic rna structurome and its functions. *Nature Reviews Genetics*, 24(3):178–196, 2023.

[14] Kalli Kappel, Kaiming Zhang, Zhaoming Su, Andrew M. Watkins, Wipapat Kladwang, Shanshan Li, Grigore Pintilie, Ved V. Topkar, Ramya Rangan, Ivan N. Zheludev, Joseph D. Yesselman, Wah Chiu, and Rhiju Das. Accelerated cryo-em-guided determination of three-dimensional rna-only structures. *Nature Methods*, 17:699–707, 2020.

[15] Helen M. Berman, John Westbrook, Zukang Feng, Gary Gilliland, T. N. Bhat, Helge Weissig, Ilya N. Shindyalov, and Philip E. Bourne. The protein data bank. *Nucleic Acids Research*, 28:235–242, 1 2000.

[16] Bohdan Schneider, Blake Alexander Sweeney, Alex Bateman, Jiri Cerny, Tomasz Zok, and Marta Szachniuk. When will RNA get its AlphaFold moment? *Nucleic Acids Research*, 51(18):9522–9532, 09 2023.

[17] Jamie J Cannone, Sankar Subramanian, Murray N Schnare, James R Collett, Lisa M D'Souza, Yushi Du, Brian Feng, Nan Lin, Lakshmi V Madabusi, Kirsten M Müller, Nupur Pande, Zhidi Shang, Nan Yu, and Robin R Gutell. The comparative rna web (crw) site: an online database of comparative sequence and structure information for ribosomal, intron, and other rnas. *BMC Bioinformatics*, 3:2, 2002.

[18] Sean R. Eddy and Richard Durbin. RNA sequence analysis using covariance models. *Nucleic Acids Research*, 22(11):2079–2088, 06 1994.

[19] Ioanna Kalvari, Eric P Nawrocki, Nancy Ontiveros-Palacios, Joanna Argasinska, Kevin Lamkiewicz, Manja Marz, Sam Griffiths-Jones, Claire Toffano-Nioche, Daniel Gautheret, Zasha Weinberg, Elena Rivas, Sean R Eddy, Robert D Finn, Alex Bateman, and Anton I Petrov. Rfam 14: expanded coverage of metagenomic, viral and microRNA families. *Nucleic Acids Research*, 49(D1):D192–D200, 11 2020.

[20] Jeffrey J. Quinn and Howard Y. Chang. Unique features of long non-coding rna biogenesis and function. *Nature Reviews Genetics*, 17(1):47–62, 2016.

[21] Sita J. Lange, Daniel Maticzka, Mathias Mohl, Joshua N. Gagnon, Chris M. Brown, and Rolf Backofen. Global or local? predicting secondary structure and accessibility in mrnas. *Nucleic Acids Research*, 2012.

[22] Beth L Nicholson and K Andrew White. Exploring the architecture of viral rna genomes. *Current Opinion in Virology*, 12:66–74, 2015. Antiviral strategies • Virus structure and expression.

[23] Christoph Flamm, Julia Wielach, Michael T. Wolfinger, Stefan Badelt, Ronny Lorenz, and Ivo L. Hofacker. Caveats to deep learning approaches to rna secondary structure prediction. *Frontiers in Bioinformatics*, 2, 2022.

[24] Kengo Sato and Michiaki Hamada. Recent trends in RNA informatics: a review of machine learning and deep learning for RNA secondary structure prediction and RNA drug discovery. *Briefings in Bioinformatics*, 24(4):bbad186, 05 2023.

[25] David H. Mathews. How to benchmark rna secondary structure prediction accuracy. *Methods*, 162-163:60–67, 2019. Experimental and Computational Techniques for Studying Structural Dynamics and Function of RNA.

[26] Kishore J. Doshi, Jamie J. Cannone, Christian W. Cobaugh, and Robin R. Gutell. Evaluation of the suitability of free-energy minimization using nearest-neighbor energy parameters for rna secondary structure prediction. *BMC Bioinformatics*, 5(1):105, 2004.

[27] Miles Kubota, Catherine Tran, and Robert C Spitale. Progress and challenges for chemical probing of rna structure inside living cells. *Nature Chemical Biology*, 11(12):933–941, 2015.

[28] Nathan A. Siegfried, Steven Busan, Greggory M. Rice, Julie A.E. Nelson, and Kevin M. Weeks. Rna motif discovery by shape and mutational profiling (shape-map). *Nature methods*, 2014.

[29] Meghan Zubradt, Paromita Gupta, Sitara Persad, Alan M. Lambowitz, Jonathan S. Weissman, and Silvi Rouskin. Dms-mapseq for genome-wide or targeted rna structure probing in vivo. *Nature Methods*, 2254:219–238, 2016.

[30] Phillip J. Tomezsko, Vincent D.A. Corbin, Paromita Gupta, Harish Swaminathan, Margalit Glasgow, Sitara Persad, Matthew D. Edwards, Lachlan Mcintosh, Anthony T. Papenfuss, Ann Emery, Ronald Swanstrom, Trinity Zang, Tammy C.T. Lan, Paul Bieniasz, Daniel R. Kuritzkes, Athe Tsibris, and Silvi Rouskin. Determination of rna structural diversity and its role in hiv-1 rna splicing. *Nature*, 582:438–442, 2020.

[31] Edoardo Morandi, Ilaria Manfredonia, Lisa M. Simon, Francesca Anselmi, Martijn J. van Hemert, Salvatore Oliviero, and Danny Incarnato. Genome-scale deconvolution of rna structure ensembles. *Nature Methods*, 18:249–252, 2 2021.

[32] David H. Mathews, Matthew D. Disney, Jessica L. Childs, Susan J. Schroeder, Michael Zuker, and Douglas H. Turner. Incorporating chemical modification constraints into a dynamic programming algorithm for prediction of rna secondary structure. *Proceedings of the National Academy of Sciences*, 101:7287–7292, 5 2004.

[33] Pablo Cordero, Wipapat Kladwang, Christopher C. Vanlang, and Rhiju Das. Quantitative dimethyl sulfate mapping for automated rna secondary structure inference. *Biochemistry*, 51:7037–7039, 9 2012.

[34] Michael F. Sloma and David H. Mathews. Improving rna secondary structure prediction with structure mapping data, 2015.

[35] Clarence Y. Cheng, Wipapat Kladwang, Joseph D. Yesselman, and Rhiju Das. Rna structure inference through chemical mapping after accidental or intentional mutations. *Proceedings of the National Academy of Sciences of the United States of America*, 114:9876–9881, 9 2017.

[36] Pablo Cordero and Rhiju Das. Rich rna structure landscapes revealed bymutate-and-map analysis. *PLOS Computational Biology*, 11:e1004473, 11 2015.

[37] Samuel W. Olson, Anne Marie W. Turner, J. Winston Arney, Irfana Saleem, Chase A. Weidmann, David M. Margolis, Kevin M. Weeks, and Anthony M. Mustoe. Discovery of a large-scale, cell-state-responsive allosteric switch in the 7sk rna using dance-map. *Molecular Cell*, 82, 2022.

[38] Grzegorz Kudla, Yue Wan, and Aleksandra Helwak. Rna conformation capture by proximity ligation. *Annual Review of Genomics and Human Genetics*, 21(1):81–100, 2020. PMID: 32320281.

[39] Jamie A. Kelly, Alexandra N. Olson, Krishna Neupane, Sneha Munshi, Josue San Emeterio, Lois Pollack, Michael T. Woodside, and Jonathan D. Dinman. Structural and functional conservation of the programmed -1 ribosomal frameshift signal of sars coronavirus 2 (sars-cov-2). *Journal of Biological Chemistry*, 295:10741–10748, 7 2020.

[40] Kaiming Zhang, Ivan N. Zheludev, Rachel J. Hagey, Raphael Haslecker, Yixuan J. Hou, Rachael Kretsch, Grigore D. Pintilie, Ramya Rangan, Wipapat Kladwang, Shanshan Li, Marie Teng Pei Wu, Edward A. Pham, Claire Bernardin-Souibgui, Ralph S. Baric, Timothy P. Sheahan, Victoria D'Souza, Jeffrey S. Glenn, Wah Chiu, and Rhiju Das. Cryo-em and antisense targeting of the 28-kda frameshift stimulation element from the sars-cov-2 rna genome. *Nature Structural & Molecular Biology*, 28:747–754, 8 2021.

[41] Chringma Sherpa, Jason W. Rausch, Stuart F.J. Le Grice, Marie Louise Hammarskjold, and David Rekosh. The hiv-1 rev response element (rre) adopts alternative conformations that promote different rates of virus replication. *Nucleic Acids Research*, 43:4676–4686, 3 2015.

[42] Anthony M. Mustoe, Nicole N. Lama, Patrick S. Irving, Samuel W. Olson, and Kevin M. Weeks. Rna base-pairing complexity in living cells visualized by correlated chemical probing. *Proceedings of the National Academy of Sciences of the United States of America*, 116:24574–24582, 11 2019.

[43] Beth L. Nicholson and K. Andrew White. Functional long-range rna–rna interactions in positive-strand rna viruses. *Nature Reviews Microbiology*, 12:493–504, 6 2014.

[44] Ewan P. Plant and Jonathan D. Dinman. The role of programmed-1 ribosomal frameshifting in coronavirus propagation, 2008.

[45] Matthew F. Allan, Amir Brivanlou, and Silvi Rouskin. Rna levers and switches controlling viral gene expression. *Trends in Biochemical Sciences*, 48, 2023.

[46] Ian Brierley, Paul Digard, and Stephen C. Inglis. Characterization of an efficient coronavirus ribosomal frameshifting signal: Requirement for an rna pseudoknot. *Cell*, 1989.

[47] J. Herald and S. G. Siddell. An 'elaborated' pseudoknot is required for high frequency frameshifting during translation of hcv 229e polymerase mrna. *Nucleic Acids Research*, 21:5838–5842, 1993.

[48] Ewan P. Plant, Gabriela C. Pérez-Alvarado, Jonathan L. Jacobs, Bani Mukhopadhyay, Mirko Hennig, and Jonathan D. Dinman. A three-stemmed mrna pseudoknot in the sars coronavirus frameshift signal. *PLoS Biology*, 3:e172, 2005.

[49] Christina Roman, Anna Lewicka, Deepak Koirala, Nan-Sheng Li, and Joseph A. Piccirilli. The sars-cov-2 programmed -1 ribosomal frameshifting element crystal structure solved to 2.09 åusing chaperone-assisted rna crystallography. *ACS Chemical Biology*, 16(8):1469–1481, 08 2021.

[50] Christopher P. Jones and Adrian R. Ferré-D'Amaré. Crystal structure of the severe acute respiratory syndrome coronavirus 2 (sars-cov-2) frameshifting pseudoknot. *RNA*, 28:239–249, 2022.

[51] Tammy C.T. Lan, Matty F. Allan, Lauren E. Malsick, Jia Z. Woo, Chi Zhu, Fengrui Zhang, Stuti Khandwala, Sherry S.Y. Nyeo, Yu Sun, Junjie U. Guo, Mark Bathe, Anders Näär, Anthony Griffiths, and Silvi Rouskin. Secondary structural ensembles of the sars-cov-2 rna genome in infected cells. *Nature Communications*, 13:1128, 3 2022.

[52] Omer Ziv, Jonathan Price, Lyudmila Shalamova, Tsveta Kamenova, Ian Goodfellow, Friedemann Weber, and Eric A. Miska. The short- and long-range rna-rna interactome of sars-cov-2. *Molecular Cell*, 80:1067–1077.e5, 12 2020.

[53] Mei Chi Su, Chung Te Chang, Chiu Hui Chu, Ching Hsiu Tsai, and Kung Yao Chang. An atypical rna pseudoknot stimulator and an upstream attenuation signal for -1 ribosomal frameshifting of sars coronavirus. *Nucleic Acids Research*, 33:4265–4275, 2005.

[54] Nuala A. O'Leary, Mathew W. Wright, J. Rodney Brister, Stacy Ciufo, Diana Haddad, Rich McVeigh, Bhanu Rajput, Barbara Robbertse, Brian Smith-White, Danso Ako-Adjei, Alexander Astashyn, Azat Badretdin, Yiming Bao, Olga Blinkova, Vyacheslav Brover, Vyacheslav Chetvernin, Jinna Choi, Eric Cox, Olga Ermolaeva, Catherine M. Farrell, Tamara Goldfarb, Tripti Gupta, Daniel Haft, Eneida Hatcher, Wratko Hlavina, Vinita S. Joardar, Vamsi K. Kodali, Wenjun Li, Donna Maglott, Patrick Masterson, Kelly M. McGarvey, Michael R. Murphy, Kathleen O'Neill, Shashikant Pujar, Sanjida H. Rangwala, Daniel Rausch, Lillian D. Riddick, Conrad Schoch, Andrei Shkeda, Susan S. Storz, Hanzhen Sun, Francoise Thibaud-Nissen, Igor Tolstoy, Raymond E. Tully, Anjana R. Vatsan, Craig Wallin, David Webb, Wendy Wu, Melissa J. Landrum, Avi Kimchi, Tatiana Tatusova, Michael DiCuccio, Paul Kitts, Terence D. Murphy, Kim D. Pruitt, O'Leary NA, Wright MW, Brister JR, Ciufo S, Haddad Haft D, McVeigh R, Robbertse Rajput B, Robbertse Rajput B, Smith-White B, Ako-Adjei D, Astashyn A, Badretdin A, Bao Y, Blinkova O, Brover V, Chetvernin V, Choi J, Cox E, Ermolaeva O, Farrell CM, Goldfarb Gupta T, Goldfarb Gupta T, Haddad Haft D, Hatcher E, Hlavina W, Joardar VS, Kodali VK, Li W, Maglott D, Masterson P, McGarvey KM, Murphy MR, O'Neill K, Pujar S, Rangwala SH, Rausch D, Riddick LD, Schoch C, Shkeda A, Storz SS, Sun H, Thibaud-Nissen F, Tolstoy I, Tully RE, Vatsan AR, Wallin C, Webb D, Wu W, Landrum MJ, Kimchi A, Tatusova T, DiCuccio M, Kitts P, Murphy TD, and Pruitt KD. Reference sequence (refseq) database at ncbi: current status, taxonomic expansion, and functional annotation. *Nucleic Acids Research*, 44:D733–D745, 2016.

[55] Gary R. Whittaker, Nicole M. André, and Jean Kaoru Millet. Improving virus taxonomy by recontextualizing sequence-based classification with biologically relevant data: the case of the ¡i¿alphacoronavirus 1¡/i¿ species. *mSphere*, 3(1):10.1128/mspheredirect.00463–17, 2018.

[56] Qiang Liu and Huai-Yu Wang. Porcine enteric coronaviruses: an updated overview of the pathogenesis, prevalence, and diagnosis. *Veterinary Research Communications*, 45(2):75–86, 2021.

[57] Chi Zhu, Justin Y. Lee, Jia Z. Woo, Lei Xu, Xammy Nguyenla, Livia H. Yamashiro, Fei Ji, Scott B. Biering, Erik Van Dis, Federico Gonzalez, Douglas Fox, Eddie Wehri, Arjun Rustagi, Benjamin A. Pinsky, Julia Schaletzky, Catherine A. Blish, Charles Chiu, Eva Harris, Ruslan I. Sadreyev, Sarah Stanley, Sakari

Kauppinen, Silvi Rouskin, and Anders M. Näär. An intranasal aso therapeutic targeting sars-cov-2. *Nature Communications*, 13:4503, 12 2022.

[58] Eva J. Archer, Mark A. Simpson, Nicholas J. Watts, Rory O'Kane, Bangchen Wang, Dorothy A. Erie, Alex McPherson, and Kevin M. Weeks. Long-range architecture in a viral rna genome. *Biochemistry*, 52(18):3182–3190, 2013. PMID: 23614526.

[59] Jong Ghut Ashley Aw, Yang Shen, Andreas Wilm, Miao Sun, Xin Ni Lim, Kum Loong Boon, Sidika Tapsin, Yun Shen Chan, Cheng Peow Tan, Adelene Y.L. Sim, Tong Zhang, Teodorus Theo Susanto, Zhiyan Fu, Niranjan Nagarajan, and Yue Wan. In vivo mapping of eukaryotic rna interactomes reveals principles of higher-order organization and regulation. *Molecular Cell*, 62:603–617, 2016.

[60] Zhipeng Lu, Qiangfeng Cliff Zhang, Byron Lee, Ryan A. Flynn, Martin A. Smith, James T. Robinson, Chen Davidovich, Anne R. Gooding, Karen J. Goodrich, John S. Mattick, Jill P. Mesirov, Thomas R. Cech, and Howard Y. Chang. Rna duplex map in living cells reveals higher-order transcriptome structure. *Cell*, 165:1267–1279, 2016.

[61] Eesha Sharma, Tim Sterne-Weiler, Dave O'Hanlon, and Benjamin J. Blencowe. Global mapping of human rna-rna interactions. *Molecular Cell*, 62:618–626, 2016.

[62] Omer Ziv, Marta M. Gabryelska, Aaron T.L. Lun, Luca F.R. Gebert, Jessica Sheu-Gruttadauria, Luke W. Meredith, Zhong Yu Liu, Chun Kit Kwok, Cheng Feng Qin, Ian J. MacRae, Ian Goodfellow, John C. Marioni, Grzegorz Kudla, and Eric A. Miska. Comrades determines in vivo rna structures and interactions. *Nature Methods*, 15:785–788, 9 2018.

[63] Timothy K Chiang, Ofer Kimchi, Herman K Dhaliwal, Daniel A Villarreal, Fernando F Vasquez, Vinothan N Manoharan, Michael P Brenner, and Rees F Garmann. Measuring intramolecular connectivity in long rna molecules using two-dimensional dna patch-probe arrays. *bioRxiv*, pages 2023–03, 2023.

[64] Jennifer K. Barry and W. Allen Miller. A -1 ribosomal frameshift element that requires base pairing across four kilobases suggests a mechanism of regulating ribosome and replicase traffic on a viral rna. *Proceedings of the National Academy of Sciences of the United States of America*, 99:11133–11138, 8 2002.

[65] Yuri Tajima, Hiro oki Iwakawa, Masanori Kaido, Kazuyuki Mise, and Tetsuro Okuno. A long-distance rna–rna interaction plays an important role in programmed - 1 ribosomal frameshifting in the translation of p88 replicase protein of red clover necrotic mosaic virus. *Virology*, 417:169–178, 8 2011.

[66] Pramod R. Bhatt, Alain Scaiola, Gary Loughran, Marc Leibundgut, Annika Kratzel, Romane Meurs, René Dreos, Kate M. O'Connor, Angus McMillan, Jeffrey W. Bode, Volker Thiel, David Gatfield, John F. Atkins, and Nenad Ban. Structural basis of ribosomal frameshifting during translation of the sars-cov-2 rna genome. *Science*, 372:1306–1313, 5 2021.

[67] Hafeez S. Haniff, Yuquan Tong, Xiaohui Liu, Jonathan L. Chen, Blessy M. Suresh, Ryan J. Andrews, Jake M. Peterson, Collin A. O'Leary, Raphael I. Benhamou, Walter N. Moss, and Matthew D. Disney. Targeting the sars-cov-2 rna genome with small molecule binders and ribonuclease targeting chimera (ribotac) degraders. *ACS Central Science*, *6*:1713–1721, 2020.

[68] Ewan P. Plant, Rasa Rakauskaitė, Deborah R. Taylor, and Jonathan D. Dinman. Achieving a golden mean: Mechanisms by which coronaviruses ensure synthesis of the correct stoichiometric ratios of viral proteins. *Journal of Virology*, 84:4330–4340, 2010.

[69] Yu Sun, Laura Abriola, Rachel O. Niederer, Savannah F. Pedersen, Mia M. Alfajaro, Valter Silva Monteiro, Craig B. Wilen, Ya-Chi Ho, Wendy V. Gilbert, Yulia V. Surovtseva, Brett D. Lindenbach, and Junjie U. Guo. Restriction of sars-cov-2 replication by targeting programmed -1 ribosomal frameshifting. *Proceedings of the National Academy of Sciences of the United States of America*, 118:e2023051118, 6 2021.

[70] Georg Wolff, Charlotte E. Melia, Eric J. Snijder, and Montserrat Bárcena. Double-membrane vesicles as platforms for viral replication. *Trends in Microbiology*, 28:1022–1033, 12 2020.

[71] Ramya Rangan, Ivan N. Zheludev, Rachel J. Hagey, Edward A. Pham, Hannah K. Wayment-Steele, Jeffrey S. Glenn, and Rhiju Das. Rna genome conservation and secondary structure in sars-cov-2 and sars-related viruses: a first look. *RNA*, 26(8):937–959, 2020.

[72] Ilaria Manfredonia, Chandran Nithin, Almudena Ponce-Salvatierra, Pritha Ghosh, Tomasz K. Wirecki, Tycho Marinus, Natacha S. Ogando, Eric J. Snijder, Martijn J. van Hemert, Janusz M. Bujnicki, and Danny Incarnato. Genome-wide mapping of sars-cov-2 rna structures identifies therapeutically-relevant elements. *Nucleic Acids Research*, 48:12436–12452, 2020.

[73] Lei Sun, Pan Li, Xiaohui Ju, Jian Rao, Wenze Huang, Lili Ren, Shaojun Zhang, Tuanlin Xiong, Kui Xu, Xiaolin Zhou, Mingli Gong, Eric Miska, Qiang Ding, Jianwei Wang, and Qiangfeng Cliff Zhang. In vivo structural characterization of the sars-cov-2 rna genome identifies host proteins vulnerable to repurposed drugs. *Cell*, 184:1865–1883.e20, 2021.

[74] Yan Zhang, Kun Huang, Dejian Xie, Jian You Lau, Wenlong Shen, Ping Li, Dong Wang, Zhong Zou, Shu Shi, Hongguang Ren, Youliang Wang, Youzhi Mao, Meilin Jin, Grzegorz Kudla, and Zhihu Zhao. In vivo structure and dynamics of the sars-cov-2 rna genome. *Nature Communications*, 12:5695, 9 2021.

[75] Nicholas C. Huston, Han Wan, Madison S. Strine, Rafael de Cesaris Araujo Tavares, Craig B. Wilen, and Anna Marie Pyle. Comprehensive in vivo secondary structure of the sars-cov-2 genome reveals novel regulatory motifs and mechanisms. *Molecular Cell*, 81, 2021.

[76] Ramya Rangan, Andrew M. Watkins, Jose Chacon, Rachael Kretsch, Wipapat Kladwang, Ivan N. Zheludev, Jill Townley, Mats Rynge, Gregory Thain, and Rhiju Das. De novo 3d models of sars-cov-2 rna elements from consensus experimental secondary structures. *Nucleic Acids Research*, 49:3092–3108, 4 2021.

[77] Siwy Ling Yang, Louis DeFalco, Danielle E. Anderson, Yu Zhang, Jong Ghut Ashley Aw, Su Ying Lim, Xin Ni Lim, Kiat Yee Tan, Tong Zhang, Tanu Chawla, Yan Su, Alexander Lezhava, Andres Merits, Lin Fa Wang, Roland G. Huber, and Yue Wan. Comprehensive mapping of sars-cov-2 interactions in vivo reveals functional virus-host interactions. *Nature Communications*, 12, 2021.

[78] Sharon Aviran and Danny Incarnato. Computational approaches for rna structure ensemble deconvolution from structure probing data. *Journal of Molecular Biology*, 434:167635, 9 2022.

[79] Michael Waskom. seaborn: statistical data visualization. *Journal of Open Source Software*, 6, 2021.

[80] Pauli Virtanen, Ralf Gommers, Travis E. Oliphant, Matt Haberland, Tyler Reddy, David Cournapeau, Evgeni Burovski, Pearu Peterson, Warren Weckesser, Jonathan Bright, Stéfan J. van der Walt, Matthew Brett, Joshua Wilson, K. Jarrod Millman, Nikolay Mayorov, Andrew R. J. Nelson, Eric Jones, Robert Kern, Eric Larson, C J Carey, İlhan Polat, Yu Feng, Eric W. Moore, Jake VanderPlas, Denis Laxalde, Josef Perktold, Robert Cimrman, Ian Henriksen, E. A. Quintero, Charles R. Harris, Anne M. Archibald, Antônio H. Ribeiro, Fabian Pedregosa, Paul van Mulbregt, and SciPy 1.0 Contributors. SciPy 1.0: Fundamental Algorithms for Scientific Computing in Python. *Nature Methods*, 17:261–272, 2020.

[81] Sara Alonso, Ander Izeta, Isabel Sola, and Luis Enjuanes. Transcription regulatory sequences and mrna expression levels in the coronavirus transmissible gastroenteritis virus. *Journal of Virology*, 76(3):1293–1308, 2002.

[82] K. Nakagawa, K.G. Lokugamage, and S. Makino. Viral and cellular mrna translation in coronavirus-infected cells. *Advances in Virus Research*, 96:165, 12 2016.

[83] Kévin Darty, Alain Denise, and Yann Ponty. Varna: Interactive drawing and editing of the rna secondary structure. *Bioinformatics*, 25:1974–1975, 2009.